Progress in Organic Coatings 174 (2023) 107280

Contents lists available at ScienceDirect

Progress in Organic Coatings

journal homepage: www.elsevier.com/locate/porgcoat

Fabrication of 8-hydroxyquinoline loaded in an aluminum-based metal-organic framework for strengthening anti-corrosion behavior of silane primer coating

Sepideh Akbaripoor Tafreshi Nejad [a], Mohammad Ramezanzadeh [a], Eiman Alibakhshi [a], Bahram Ramezanzadeh [a], Marie-Georges Olivier [b,*], Mohammad Mahdavian [a,*]

[a] Department of Surface Coating and Corrosion, Institute for Color Science and Technology, Tehran, Iran
[b] Department of Materials Science, Faculty of Engineering, University of Mons, Place de Parc, 20, 7000 Mons, Belgium

ARTICLE INFO

Keywords:
MOF
MIL-53_{as}(Al)
Galvanized steel
Silane
Epoxy
Corrosion

ABSTRACT

In this article, MIL-53_{as}(Al) metal-organic framework (MOF) was synthesized and loaded with 8-hydroxyquinoline (8HQ) as a corrosion inhibitor. The characterization based on FTIR, Raman, XRD, and XPS confirmed the successful loading of 8HQ in MOF. The corrosion inhibitive activity of the products was studied in the solution phase, single silane coating, and duplex coating system consisting of hybrid silane primer and epoxy topcoat applied on galvanized steel. XPS confirmed chemisorption of released 8HQ from the MIL-53_{as}(Al) on the metal surface. Electrochemical test results revealed a significant improvement in corrosion protection of single layer and duplex coating systems in the presence of 8HQ-doped MOF.

1. Introduction

The protection of metals against corrosion is one of the big challenges for industries. For many years, conventional methods such as cathodic/anodic protection, anti-corrosion fillers, corrosion inhibitors, and coatings were used to protect metal against corrosion. A combination of two or three of these methods could provide both active/barrier anti-corrosion behaviors to protect metals from corrosion attacks for the long term [1]. However, the direct application of inhibitors in the coating may decline its barrier capability due to the interference in curing reaction [2]. Therefore, the corrosion inhibitors loaded containers have been incorporated into the coatings to enhance the coatings' barrier and active protection capabilities [3,4]. Graphene oxide (GO) [5,6], carbon nanotubes (CNTs) [7,8], layered double hydroxides (LDHs) [9,10], molybdenum disulfide (MoS_2) [11,12], covalent organic frameworks (COFs) [13,14], and Mxenes [15,16] are some of the most novel and interested corrosion inhibitor containers. Ashraf Ismail et al. conducted a research concerning application of halloysite nanotubes for loading benzotriazole, sodium benzoate, and lauric acid which was further used for reinforcing the anticorrosion behavior of epoxy coating [17]. Following the rapid growth in the fabrication of novel anti-corrosive fillers, corrosion inhibitor containers based on porous coordination polymers (PCPs) have been developed. As one of the major categories of PCPs, metal-organic frameworks (MOFs) have made researchers interested in using them in the different application areas in the last decade [18]. MOFs can be constructed by coordinating metal-containing clusters named secondary building units (SBUs) with organic ligands through strong bonds. Having some unique properties, e.g., high internal surface area (even up to 6000 m^2/g), large pore volume (about 3.0 cm^3/g) [19], thermal stability [20], crystalline structures [21], and hybrid organic/inorganic composition [22], MOFs are suitable for various applications in the chemical and physical fields. Due to the fascinating and diverse structural properties, new applications for MOFs have been emerged over time, such as optics, catalysis, adsorption, sensing, drug delivery, thin films, and anti-corrosion fillers [18]. There are many reports on the application of different kinds of porous MOFs and modified MOFs as anti-corrosion fillers and pigments [23–25], corrosion inhibitors [26,27], and thin-film [28,29]. As a case study, Duan et al. [30] used the microemulsion method to prepare Zeolitic imidazolate framework-8 (ZIF-8) as an active nanofiller. They observed a high anti-corrosion performance for the synthesized ZIF-8 nanoparticles in the epoxy coating. Ramezanzadeh et al. [31] constructed Zr-based MOFs (NH_2-UIO-66) covalently functionalized by glycidyl methacrylate as a novel anti-corrosion filler with excellent anti-corrosion

---

* Corresponding authors.
E-mail addresses: marjorie.olivier@umons.ac.be (M.-G. Olivier), mahdavian-m@icrc.ac.ir (M. Mahdavian).

https://doi.org/10.1016/j.porgcoat.2022.107280
Received 16 August 2022; Received in revised form 13 October 2022; Accepted 19 October 2022
Available online 27 October 2022

effects (active/barrier) in the epoxy coating. Zhao et al. [32] constructed a high-performance polyvinyl butyral (PVB) coating through the incorporation of GO decorated with zinc-based MOF (GO/ZIF-8) container loaded with benzotriazole (BTA). Chen et al. [33] selected GO/NH_2-UIO-66 to encapsulate BTA as a novel anti-corrosion filler in the epoxy coating.

It has been shown that 8HQ is one of the efficient inhibitors for galvanized steel. Kartsonakis et al. undertook a study comparing the corrosion protection of hot-dip galvanized (HDG) steel in the saline solution containing various inhibitors. The results indicated that 8HQ and $Ce(NO_3)_3$, depict the highest inhibition efficiency value [34]. In a study conducted by Taryba et al., different submicron containers were used for loading corrosion inhibitors. In particular, titania particles were used as containers for loading 8HQ in order to modify primer coatings. The self-repairing capability of the thin coatings was then investigated, proving low corrosion activity of the specimen modified with 8HQ loaded titania [35].

Wang et al. loaded 8-hydroxyquinoline (8HQ) corrosion inhibitor into halloysite nanotubes (HNTs) and encapsulated by Cu-8HQ complex stopper to reinforce anti-corrosion behavior of epoxy coatings. The results indicated higher resistance of Cu-8HQ@HNTs/epoxy coating [36].

In this work, for the first time, an aluminum-based MOF has been utilized as a novel corrosion inhibitor container for loading of 8HQ. MIL-53_{as}(Al) is one of the well-known porous aluminum (Al) based metal-organic frameworks (Al-MOF). The chemical stability of the porous MOFs is one of the critical features for the loading of corrosion inhibitors. MOFs must be stable during the loading of corrosion inhibitors. Also, they have to be stable enough after incorporation into the coating to provide both active/barrier protection in the coatings. The Al-cluster coordinated with carboxylate linkers is one of the most chemically and thermally stable MOFs [37], which makes it a good candidate for loading corrosion inhibitors. In this study, the MIL-53as(Al) container was constructed by coordinating Al as a metal cluster with terephthalic acid as an organic linker. FT-IR, Raman, XRD, and FE-SEM were employed to characterize the prepared MIL-53_{as}(Al) powder. MIL-53_{as}(Al) was then loaded with 8HQ to provide active inhibition properties for silane coating on the electro-galvanized steel (EGS) panels. The corrosion inhibition properties were assessed (a) in the solution phase on bare samples, (b) on single layer silane coated samples, and (c) on the duplex silane-epoxy coated samples.

2. Experimental section

2.1. Materials

Commercial EGS panels produced through a batch galvanizing process were purchased from Gheteh Pooshesh Kar (Iran). The thickness of the zinc layer was about 2.5 μm, and the dimension of the EGS panels was 10 cm × 3 cm. Terephthalic acid, 3-(chloropropyl)-trimethoxysilane (CPTMS), tetraethylorthosilicate (TEOS), and 8-hydroxyquinoline (8HQ) were supplied by Merck Millipore. Aluminum nitrate nonahydrate and dimethylformamide (DMF) were acquired from Sigma-Aldrich and Exir GmbH. Acetyl acetone (AcAc) was obtained from Sigma-Aldrich. Nitric acid (65 %) and ethanol 96 % were purchased from Mojallali Industrial Chemical Complex. Epoxy resin E06 and polyamine epoxy hardener (PC205) were procured from Sana Shimi.

2.2. Premodification of EGS panels

The premodification process of the EGS panel embodied the following steps: (1) removal of contaminants from the surface of EGS panels using acetone; (2) modifying the clean panels in an alkaline bath (0.5 M NaOH+ 2 wt% AcAc) for 5 min at 50 °C [38]; (3) washing the EGS specimens with tap water and DI water; (4) drying the panels using compressed air stream.

2.3. Synthesis of MIL-53_{as}(Al) metal-organic framework

In order to synthesize MIL-53_{as}(Al) denominated as MOF, Al $(NO_3)_3.9H_2O$ (1.182 g), terephthalic acid (0.777 g), and DMF (60 ml) were mixed for 30 min prior to transforming to a 100 ml sealed autoclave. The autoclave was kept at 130 °C for 72 h. After cooling it down to ambient temperature, a white precipitate was collected using centrifugation by DMF and ethanol [37].

2.4. Synthesis of 8HQ loaded MOF

A saturated solution of 8HQ in DI water was prepared by adding 8HQ (0.0555 g) to DI water (100 ml) under continuous stirring for 2 h. After complete dissolution of 8HQ powder and obtaining a clear yellow solution, 0.0555 g of MIL-53_{as}(Al) was added to the prepared precursor solution in one shot and was stirred for 24 h. Then, the mixture was centrifuged several times using an abundant amount of water to remove reactant remnants and dried at 60 °*C*.

2.5. Preparation of sol-gel coating

Silanization was accomplished using a bath containing CPTMS (9.75 % *v*/v), TEOS (30.2 % v/v), DI water (5.6 % v/v), ethanol (54.2 % v/v), and nitric acid (0.14 % v/v). The solution was stirred for 24 h at ambient temperature. In order to prepare silane coating containing MOF and inhibitor-loaded MOF (MOF + 8HQ), 0.2 % of the aforementioned materials (in reference to the total amount of TEOS+CPTMS) was added to the neat silane coating and stirred until complete dispersion. Subsequently, EGS panels were dip-coated at a speed of 100 mm/min, and the panels were dried at room temperature for a day, and the post-curing was conducted at 150 °C for 30 min. In addition, the dispersion stability of MOFs in the silane solution was visually examined after 8 h preparation of dispersions.

2.6. Preparation of duplex coating system

Epoxy coating (resin: hardener, 1:0.5) was applied to the cured silane coatings using a spray gun system. The coated specimens were left at room temperature for a day. Then, the curing was accomplished through heating at 80 °C for an hour. The dry film thickness of the samples was 70 ± 10 μm measured using a coating thickness gauge.

2.7. Techniques

Perkin Elmer IR spectrometer (Spectrum one, USA) was utilized to perform Fourier Transform Infrared Spectroscopy (FTIR) analysis within the range of 4000–450 cm^{-1}. A smidgen amount of MOF and inhibitor-loaded MOF was ground, mixed with KBr, and pressed into a pellet to prepare the FTIR specimen. Wide-angle diffraction Philips X-ray (XRD) spectrometer (PW1730 model, Cu Kα radiation, 1.54 Å) was used for crystallography studies in the range of $2\theta=10–80°$. Raman analysis was conducted using an XploRA Plus instrument equipped with a 785 nm laser. X-ray photoelectron spectroscopy (XPS, 8025-BesTec) was implemented using Al Kα radiation.

Brunauer-Emmett-Teller (BET) analysis was performed at 77 K (BELSORP- MINI II, Japan). The degassing process was performed at 150°C under a vacuum (BEL PREP VAC II).

Thermal gravimetric analysis was conducted using TGA equipment (SDTQ600, TA, USA) scanning from ambient temperature to 600 °C with heating rate of 10 °C/min at Argon atmosphere.

Transmission Electron Microscopy analysis was performed using TEM instrument (EM208S, Philips) with operating voltage of 100 kV.

Organic compound concentration of the extract solutions was measured using total organic carbon (TOC) analyzer (TOC-L, SHIMADZU). Extract solution of 8HQ loaded MOF at a concentration of 1000 ppm was prepared. After 24 h of stirring, the sample was

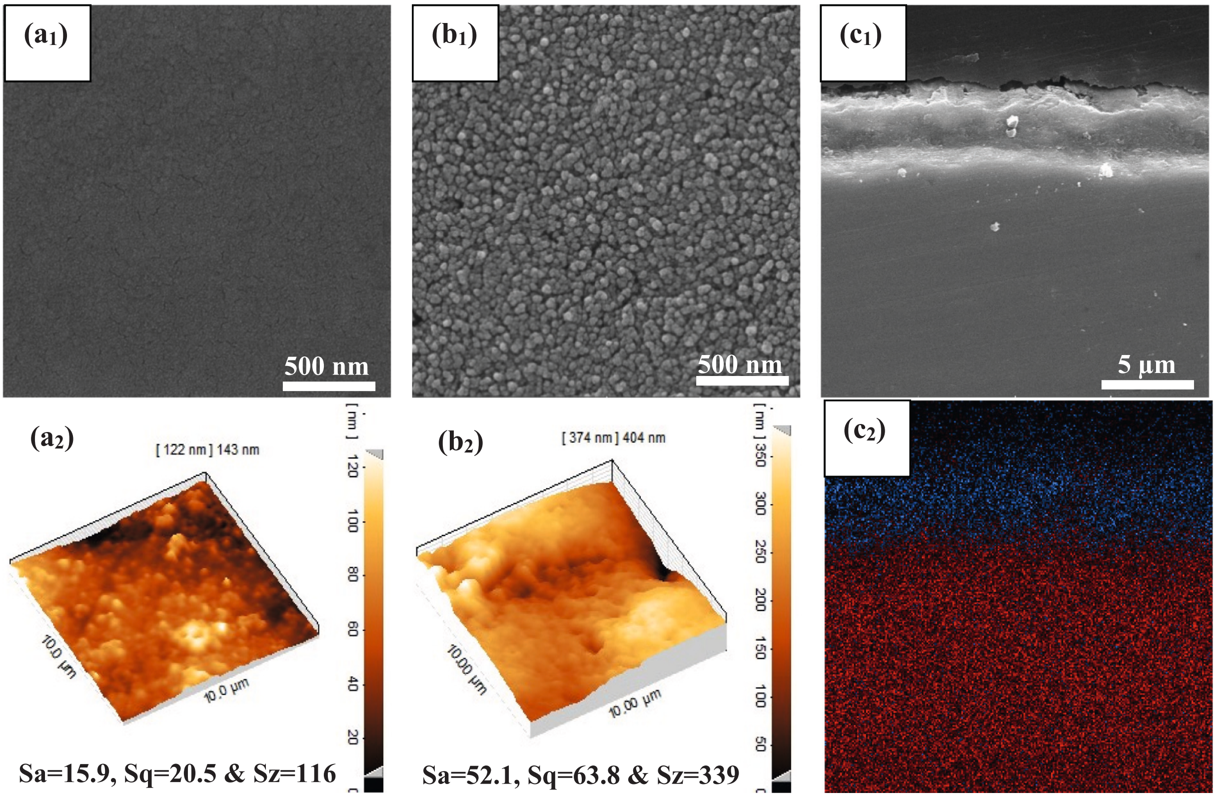

Fig. 1. FE-SEM micrograph (a_1 and b_1), corresponding AFM images (a_2 and b_2) of the unmodified EGS (a_1 and a_2) pre-modified EGS, (b_1 and b_2) and cross section FE-SEM micrograph of unmodified EGS (c_1) and combined map analysis of Zn (blue color) and Fe (red color) elements (c_2). (For interpretation of the references to color in this figure legend, the reader is referred to the web version of this article.)

centrifuged and the supernatant was used for further analysis.

Field emission scanning electron microscopy (FE-SEM, Tescan Mira3, Czech Republic) was implemented to study the silanized samples' morphology and surface coverage prior to and after exposure to NaCl 3.5 %. It was also used to analyze the scratched area of the duplex coating system and coatings thickness. Energy dispersive spectroscopy (EDS) coupled with FE-SEM was employed for the elemental analysis.

The electrochemical study of the specimens in the solution phase was scrutinized through polarization and electrochemical impedance spectroscopy (EIS) techniques employing Ivium compactstat equipment in a three-electrode configuration encompassing a saturated calomel electrode (reference), a platinum electrode (counter), and the samples (working electrode) with a 1 × 1 cm^2 exposure area. To prepare the test solutions, 1 g of MOF and MOF + 8HQ were separately added to 1 l of 3.5 % NaCl solution and stirred for a day. Then, the dispersions were centrifuged, and supernatant solutions were used as the test solutions. EIS was recorded within the frequency range of 10^{-2}–10^4 Hz and using a perturbation of 10 mV vs. open circuit potential (OCP). Polarization was conducted at a scan rate of +0.5 mV/s within the potential span of ±160 mV vs. OCP. The EIS was also performed on silane-coated specimens immersed in a 3.5 % NaCl medium. The scratched duplex coating system (silane + epoxy) was evaluated by EIS and electrochemical noise measurements (ENM). Wavelet transform (WT) was utilized to evaluate the electrochemical current noise (ECN) signals. In order to evaluate the ECN signals, two nominally identical duplex coated samples with a 2 × 2 cm^2 area encompassing a scratch with a length of 15 mm, and a width of 100 µm were used.

Table 1
EDX results of unmodified and pre-modified EGS panels.

Sample	O	Zn
Unmodified EGS	3.4	96.6
Pre-modified EGS	37.5	64.7

3. Results and discussion

3.1. Characterization of unmodified and pre-modified EGS panels

Fig. 1 represent FESEM micrographs and AFM images taken from unmodified and pre-modified EGS panels providing an analogy between the two samples. Fig. 1$\mathbf{a_1}$ and $\mathbf{b_1}$ confirm the morphology changes caused by the alkaline premodification. EDS results tabulated in Table 1 affirm the alteration of surface composition as a result of alkaline modification. AFM images Fig. 1$\mathbf{a_2}$ and $\mathbf{b_2}$ represent the topography of the samples. According to the results, the surface of the unmodified EGS panel is smoother, while the alkaline premodification has led to roughness increment. Surface parameters, including *Sa* (arithmetical mean height), *Sz* (maximum height), and *Sq* (root mean square height), are also provided below the corresponding AFM images.

The cross-sectional FESEM micrograph of the unmodified EGS panel and corresponding map analysis are provided in Fig. 1$\mathbf{c_1}$ and $\mathbf{c_2}$, respectively. According to the outcome data and distribution of Fe and Zn elements throughout the investigated sector, the thickness of the zinc layer is distinguished and estimated to be 3.1 ± 0.3 µm.

3.2. Characterization of MOF and MOF + 8HQ

A schematic structure of the synthesized MOF has been presented in Fig. 2a. This figure shows the metallic centers of this MOF, i.e.,

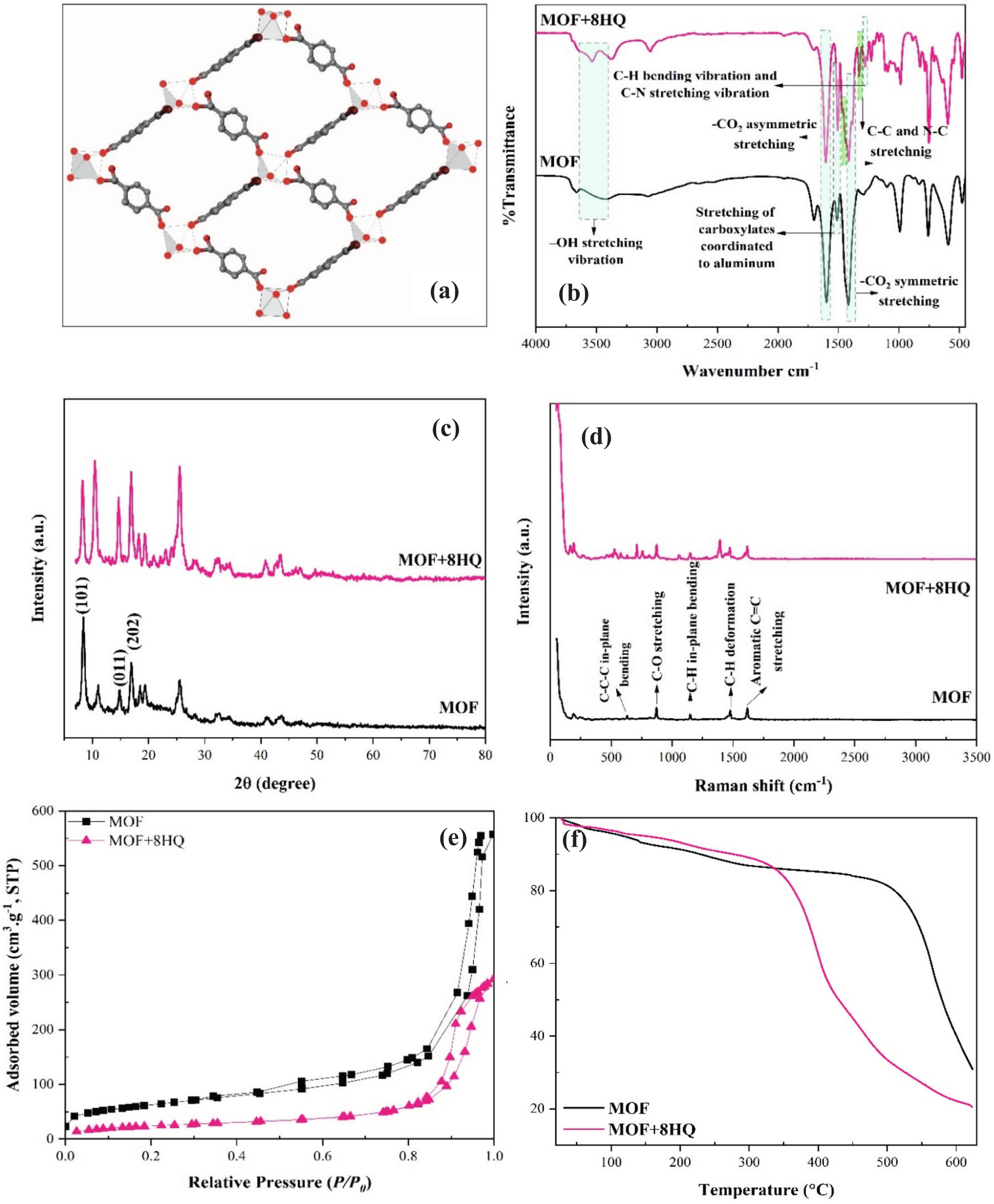

Fig. 2. 3D structure of MIL53$_{as}$ (Al), Gray octahedral: $AlO_4(OH)_2$; gray circles: carbon; red circles: oxygen (a), FTIR spectra: MOF, MOF + 8HQ (b), XRD diffractograms: MOF, MOF + 8HQ (c), Raman spectra of MOF and 8HQ loaded MOF (d), BET plots: MOF, MOF + 8HQ (e) and TGA diagrams of MOF and 8HQ loaded MOF (f). (For interpretation of the references to color in this figure legend, the reader is referred to the web version of this article.)

$AlO_4(OH)_2$, connected with terephthalic acid ligand forming rhombic tunnels [39]. Fig. 2b manifests the FTIR spectra of MOF and 8HQ loaded MOF. Both spectra reveal the peaks around 1417 cm^{-1} and 1597 cm^{-1} ascribed to —CO_2 symmetric and asymmetric stretching, respectively [40]. The absorption band at ca. 1511 cm^{-1} is assigned to the stretching of carboxylates coordinated to aluminum [39]. The peak positioned at around 3535 cm^{-1} is due to the —OH stretching vibration bands of water molecules or surface hydroxyl groups [41]. FTIR spectrum of 8HQ loaded MOF shows distinct peaks from MOF spectrum. The peak at 1280 cm^{-1} is attributed to the C—H bending vibration and C—N stretching vibration [42,43]. The peaks at 1327.9 cm^{-1}, 1468.1 cm$^{-1,}$ and 1505.3 cm^{-1} represent the stretching of the C—C, and N—C bonds, originating from the aromatic ring structure of 8HQ [44]. The FTIR results depict the successful loading of 8HQ within the MOF structure.

The diffractograms of MOF and 8HQ loaded MOF are shown in Fig. 2c. The results obtained from the reference MOF show good conformity with the CCDC 220475 diffraction pattern, where the main bands at ca. 8.4, 14.7, and 17° are related to (101), (011), and (202) planes of MIL-53$_{as}$(Al) [42], confirming successful synthesis of MOF structure. The results indicate the retention of characteristic peaks of MOF after incorporation of 8HQ. However, the relative intensity of the peaks at ca. 10 and 14.6° has been intensified, which can be attributed to

Table 2
BET parameters determined from MOF and MOF + 8HQ samples.

Sample	$a_{s,\ BET}$ (m^2g^{-1})	Mean pore diameter (nm)	Total pore volume (cm^3g^{-1}) ($p/p_0 = 0.990$)
MOF	220.77	15.265	0.8425
MOF + 8HQ	87.547	19.99	0.4375

the presence of 8HQ [44,45] and is related to (220) and (400) planes of 8HQ, respectively according to JCPDS card #39-1857 [46].

Fig. 2d reveals Raman spectra of the MOF and 8HQ loaded MOF. The characteristic peaks of MOF at 628, 870, 1145, 1473, and 1615 cm^{-1} attributed to C—C—C in-plane bending of the aromatic ring, C—O stretching, C—H in-plane bending, C—H deformation, and aromatic C═C stretching [47], evidenced successful synthesis of MOF. Intense 8HQ peaks at 671, 1337, and 1537 cm^{-1} appeared in the 8HQ-loaded MOF [48], confirming 8HQ loading in the MOF consistent with the FTIR and XRD results.

The porous structure of the samples was investigated through N_2 adsorption-desorption isotherm. Fig. 2e represents BET plots of MOF and MOF + 8HQ samples. Both samples revealed a hysteresis loop upon desorption. Based on the resultant data, in the case of the MOF + 8HQ sample, surface area and total pore volume have been decreased due to the loading of inhibitor, as a matter of course. The samples showed typical type IV isotherm. The porosimetry data are collected in Table 2. At relatively high (P/P_0), the higher amount of N_2 adsorption can be

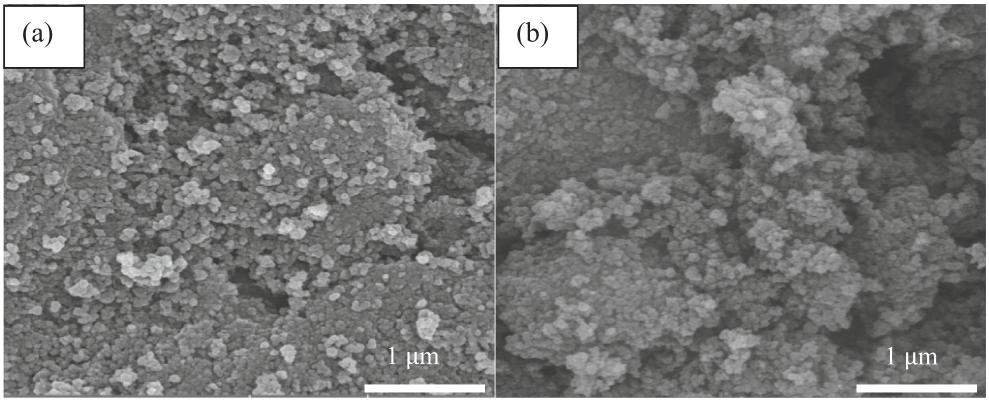

Fig. 3. FESEM micrographs: MOF (a), MOF + 8HQ (b).

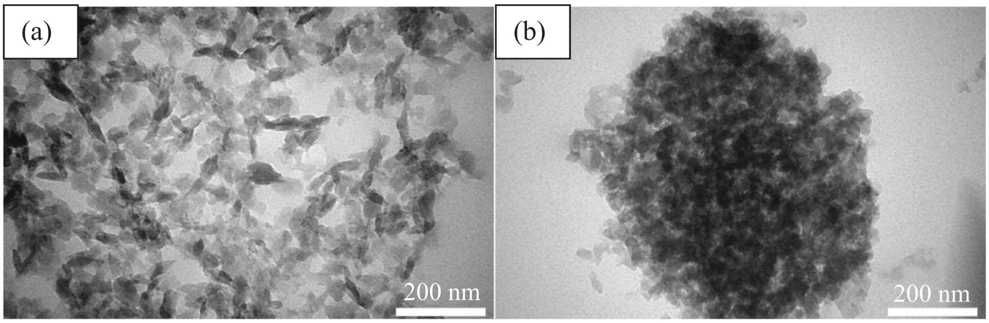

Fig. 4. TEM images: MOF (a), MOF + 8HQ (b).

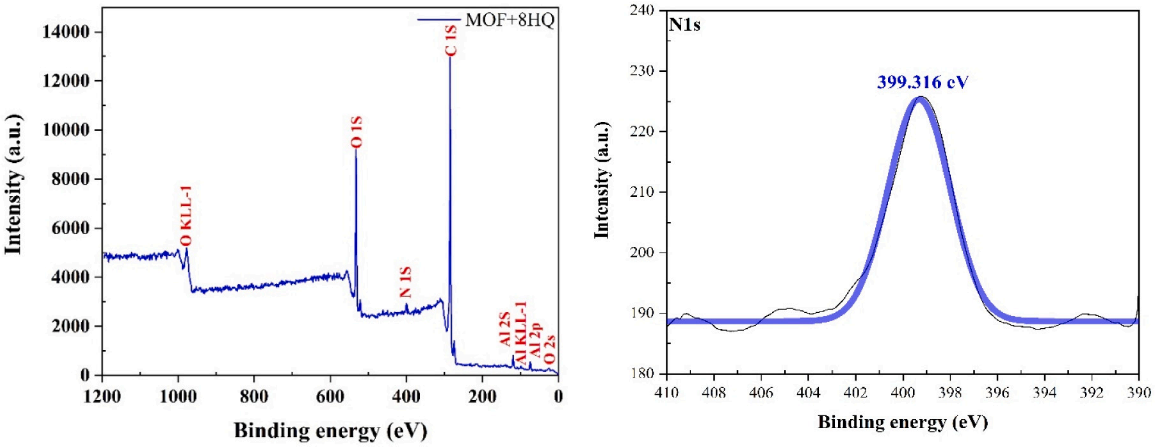

Fig. 5. XPS survey and high-resolution N 1 s spectra of the inhibitor loaded MOF (MOF + 8HQ).

Table 3
Element atom percentages of MOF + 8HQ extracted from XPS survey.

Peak ID	Atom (%)
O 1s	12.1
N 1s	2.2
C 1s	70.5
Al 2s	3.6
Al KLL-1	2.1
Al 2p	3
O 2s	6.5

ascribed to accumulated pores [37].

TGA diagrams of MOF and MOF + 8HQ are provided in Fig. 2f. In case of MOF curve, the lower temperature weight loss which occurred at around 100–200 °C is caused by removal of guest molecules (water and DMF) while the higher temperature weight loss (around 500 °C) can be ascribed to the decomposition of terephetalic acid ligand [49]. In case of MOF + 8HQ sample more weight loss can be due to the decomposition of the adsorbed 8HQ. Degradation of 8HQ takes place until 212 °C [50]. The retardation of 8HQ decomposition in 8HQ loaded sample in comparison to pure 8HQ (about 100 °C) is caused by the loading of 8HQ in MOF which in turn can provide protection due to more thermally-stability of MOF. The difference between weight loss at 622 °C is about 10.8 % for the samples which can provide an approximate estimation of the loaded 8HQ.

Fig. 3 shows micrographs taken from MOF and 8HQ loaded MOF. Fig. 3a depicts a lump of semi-spherical particles with variable sizes around 40 nm. Fig. 3b represents a minor deviation from the initial morphology and reduced sharpness of particle boundaries which may be due to the adsorption of 8HQ on the surface of the particles.

Fig. 4 depicts the TEM micrographs of the samples. The morphology of the samples is in good conformity to the corresponding SEM micrographs provided in Fig. 3. The dark areas in Fig. 4b may be attributed to the loading of 8HQ.

The XPS survey spectrum along with the high-resolution N 1 s spectrum obtained from the MOF + 8HQ sample, are provided in Fig. 5. The presence of N in the MOF + 8HQ sample clearly indicates the successful loading of 8HQ in the MOF structure. The atomic composition of the elements derived from the XPS spectrum is listed in Table 3. Based on this table, the atomic percentage of nitrogen in the MOF + 8HQ sample is 2.2 %, giving a rough estimation of the 8HQ loading level in MOF. The high-resolution N1s spectrum shows only one peak at 399.3 eV, related to pyridinic nitrogen [51]. The absence of the peak around 396.5 eV attributed to N—Al bonds [52] indicates that 8HQ has only been physically trapped in the MOF pores, and no chemical reaction between 8HQ and MOF has occurred.

The extract of MOF + 8HQ was examined by TOC to assess the concentration of the released 8HQ. The results indicated a TOC of 139.8 ppm. Considering the concentration of MOF + 8HQ, which was 1000 ppm, the release extent of 8HQ in the test solution was about 14 wt% of MOF + 8HQ. Based on the TGA analysis, 8HQ forms around 10.8 wt% of MOF + 8HQ. Therefore, around 22.8 wt% of the released organic species originated from MOF scaffold, i.e., terephthalic acid, and the rest belongs to 8HQ.

3.3. *Dispersion stability of the prepared silane coatings*

The dispersion stability of silane samples after 8 h was investigated through visual evaluation provided in Fig. 6. According to the results (Fig. 6b and Fig. 6c), silane coating containing MOF and the one containing MOF + 8HQ both retained dispersion stability, and there were no detectable precipitation and agglomeration which guarantees the durability of the prepared coatings within the working time.

3.4. *Corrosion studies*

3.4.1. *Solution phase*

The EIS and polarization tests were utilized to assess the inhibition effectiveness of MOF and MOF + 8HQ on bare EGS samples. The impedance Bode plots for the blank (the reference saline solution containing no inhibitor), MOF, and MOF + 8HQ test solutions collected over a 48 h exposure period are shown in Fig. 7.

The corrosion inhibition efficacy of materials can be determined using the Bode diagram's low-frequency impedance (*BLFI*) [53]. The BLFI has decreased throughout the entire exposure time for the sample immersed in the uninhibited solution, revealing its poor corrosion resistance. Corrosion initiation and the subsequent formation of corrosion products rapidly occurred on the reference sample's surface. Throughout the immersion period, the MOF has a slightly greater BLFI than the reference sample, as shown in the diagrams. This suggests that at the interface, a mild inhibitory action was elicited by MOF. From Fig. 7, it is easy to see how the BLFI rises after applying MOF + 8HQ, which is correlated to the release and chelating action of 8HQ molecules.

Bode-Phase diagrams can be used to clarify corrosion responses at the metal-solution interface [54]. At the early immersion times (1 and 24 h), a single time constant has been discovered in the case of the blank specimen ascribed to the electrical double layer. At longer immersion times (48 h), the manifestation of a second time constant is associated with the O element known as open finite length diffusion (OFLD). When it comes to the inhibited samples, however, two or three constants have been identified. Each of the three-time constants relates to a different phase of formation of an inhibitive film or an oxide layer (high-frequency), and an electrical double layer (medium-frequency) and diffusion [54].

The diameter of the semicircles in Nyquist diagrams rises when the corrosion inhibitor is introduced to the solution, as can be seen in **Supplementary Information** (**Fig. S1**). The diameter expansion at the

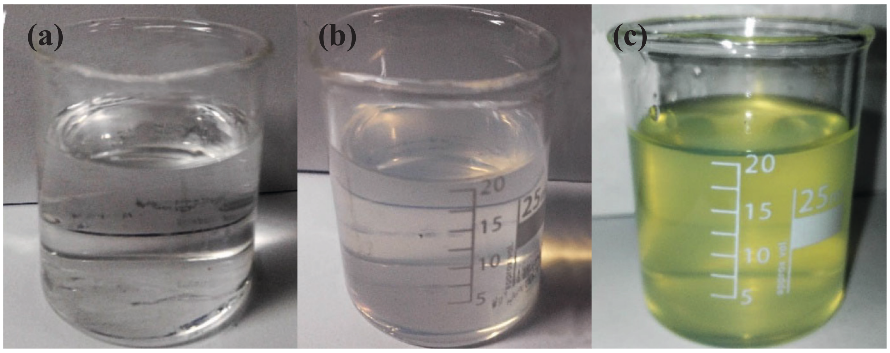

Fig. 6. Visual evaluation of dispersion stability of the prepared silane coating; Neat silane (a), silane containing MOF (b), and silane containing MOF + 8HQ (c) after 8 h.

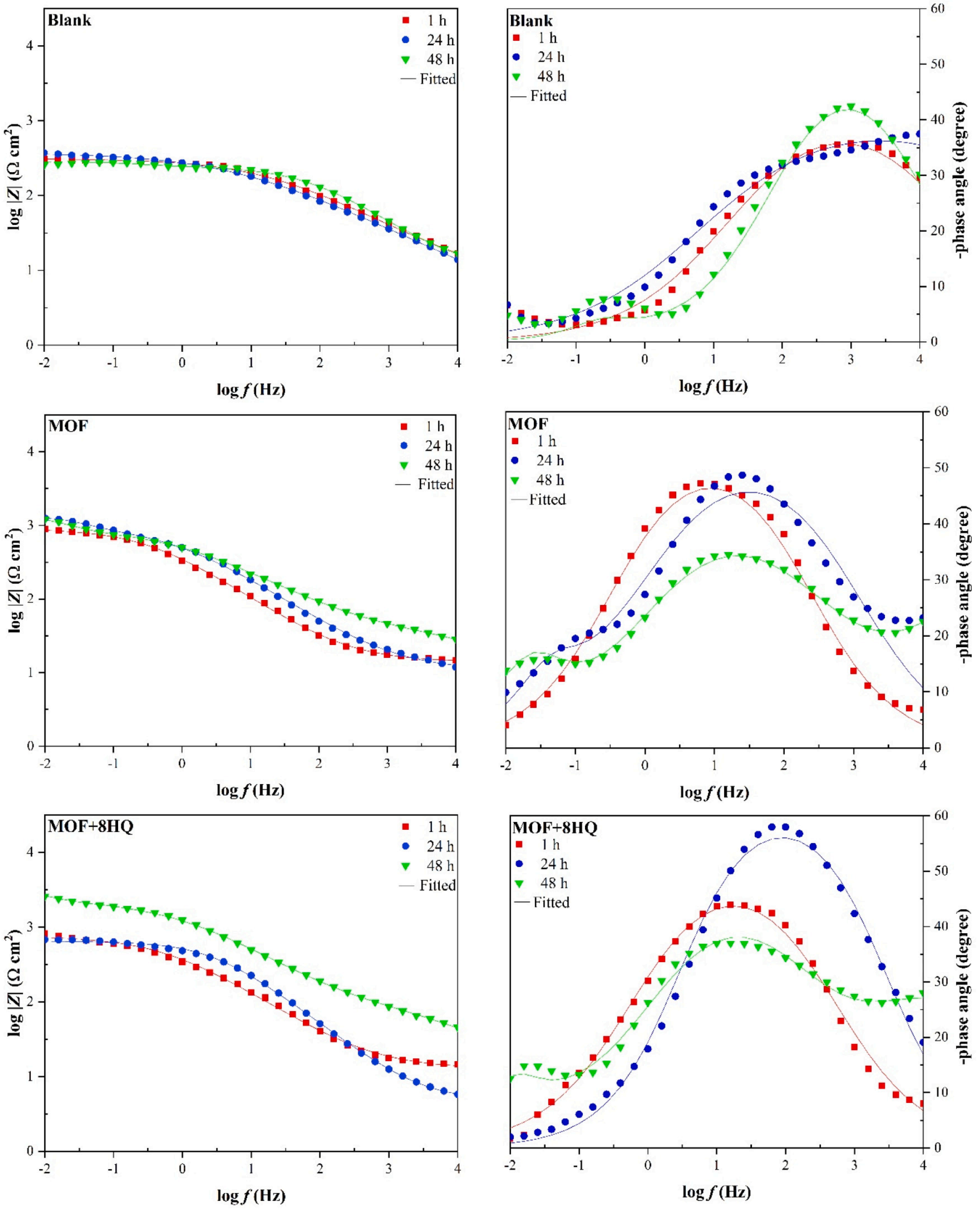

Fig. 7. Bode impedance module (left) and phase angle (right) plots of the samples immersed in (a) 3.5 % NaCl (blank), (b) MOF, and (c) MOF + 8HQ test solutions.

end of immersion is not substantial when MOF is inserted, but when the 8HQ is loaded into the MOF structure, the diameter aggrandizes, especially after 48 h immersion. In other words, a larger radius of MOF + 8HQ compared to MOF indicates that its inhibition performance is improved.

Fig. 8 shows equivalent electrical circuits. The film resistance (R_f), electrolyte resistance (R_s), charge transfer resistance (R_{ct}), constant phase elements (CPEs) of the film and electrical double layer and O element were used to build the electrical circuits to fit the EIS data. The fitting results also derived the admittance (Y) and the exponent (n) of CPEs. In order to monitor the inhibition efficiency of the samples, Eq. (1) was used [55]:

$$\eta\,(\%) = \frac{R_t^i - R_t^0}{R_t^i} \times 100 \tag{1}$$

where R_t^i and R_t^0 denote total resistance of the sample in the presence and absence of inhibitors, respectively.

Table 4 contains a summary of all of the quantitative outcomes of the EIS fitting and inhibition efficiency values.

It is well acknowledged that the inhibition activity of materials can be predicted from the sum of their resistances (total resistance, R_t). In the case of blank, the R_t ($R_{ct} + R_{ox} + R_f$) was the lowest during the immersion stages. The MOF sample showed improved resistance compared to the blank one elucidating the oxide film development on the surface

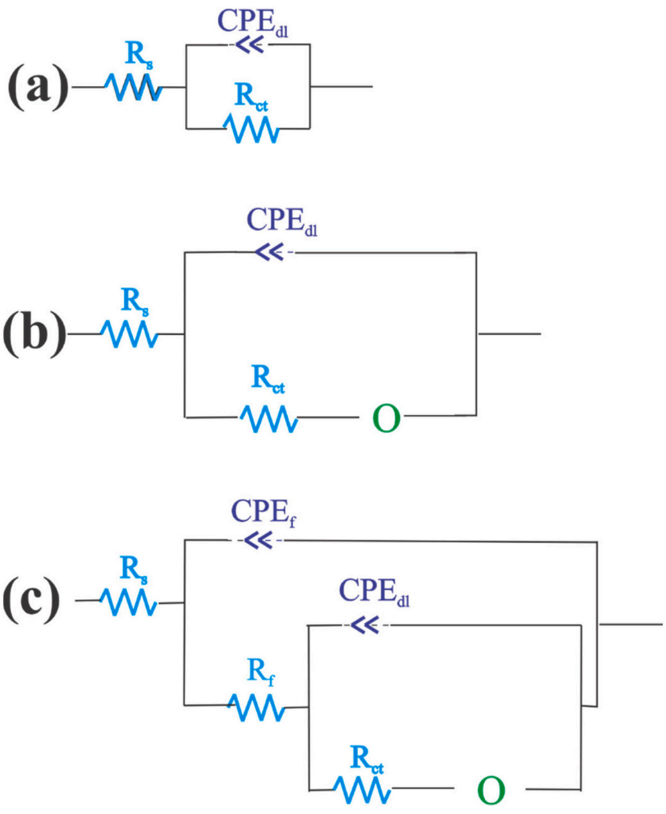

Fig. 8. Electrical equivalent circuits for simulating the EIS spectra.

and then decreasing. It can be concluded that the partial release of metal cations and terephthalic acid from the MOF scaffold led to inhibitive behavior. The R_t values of the MOF + 8HQ sample are higher than the MOF, meaning that the loading of the inhibitor (8HQ) into the MOF structure has boosted the corrosion inhibition. The R_f of the MOF + 8HQ sample is higher than that for the MOF at the end of the immersion time, reflecting its good protection function. This may be because of the zinc and 8HQ interaction at the surface-active location, building an inhibitive layer on the surface.

The polarization test was utilized to acquire a better grasp of the corrosion inhibition mechanism. The exemplary polarization curves of the coated specimens after 48 h immersion in the test solutions are shown in Fig. 9 The i_{corr} (corrosion current density) derived using Tafel extrapolation were 7.9, 3.6, 2.8 μAcm^{-2}, respectively.

From Fig. 9, it can be concluded that MOFs depressed both the anodic and cathodic branches, confirming the mixed inhibition action of the MOFs. The MOF + 8HQ sample showed a considerable reduction in i_{corr} compared to the MOF sample. In other words, the lowest i_{corr} of the MOF + 8HQ sample confirms its best corrosion inhibition capabilities. It has to be noted that at high anodic potentials, there is a sharp increase in current densities implying rupture of the film formed on the EGS. Such a rupture occurs at higher anodic polarization for the MOF + 8HQ indicating its more film stability compared to the one formed in the presence of MOF. It seems that the carboxylic acid ligands liberated from the MOF structure are responsible for the loss of surface film stability at high anodic potentials. Similar behavior has been observed in the presence of carboxylic acid-based corrosion inhibitors in the literature [56,57].

The FESEM was used to investigate the establishment of an inhibitive layer on the EGS substrate. Fig. 10 shows the FESEM micrographs of samples surface after 48 h immersion in 3.5 % NaCl containing MOF and MOF + 8HQ extract.

Corrosion products are seen in the FESEM micrographs of bare EGS

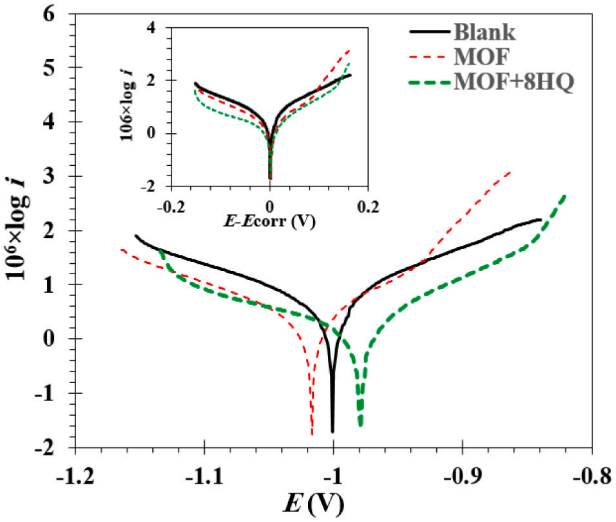

Fig. 9. Polarization diagram of the GS samples immersed for 48 h in the 3.5 % NaCl (blank), MOF, and MOF + 8HQ test solutions. The normalized curves based on E_{corr} are provided in the inset diagram.

Table 4
Variation of EIS electrochemical parameters of samples immersed in 3.5 % NaCl, MOF and MOF + 8HQ extract during 48 h.

Sample	Time (h)	R_{ct} [a] ($\Omega.cm^2$)	$Y_{0,dl}$ [b] ($\mu s^n.\Omega^{-1}.cm^{-2}$)	n_{dl} [c]	R_f [d] ($\Omega.cm^2$)	$Y_{0,f}$ [e] ($\mu s^n.\Omega^{-1}.cm^{-2}$)	n_f [f]	Yo [g] ($ms^n.\Omega^{-1}.cm^{-2}$)	B [h] ($ms^{1/2}.cm^{-2}$)	R_t [i] ($\Omega.cm^2$)	η (%)
Blank	1	301.3	247.6	0.53	–	–	–	–	–	301.1	–
	24	364.3	476.8	0.46	–	–	–	–	–	364.3	–
	48	236.7	73.4	0.65	–	–	–	37.3	1.3	236.7	–
MOF	1	885.1	678.8	0.64	–	–	–	–	–	885.1	66
	24	885.8	395.2	0.61	–	–	–	6.8	3.1	885.8	58.9
	48	769.7	369.5	0.55	37	40.8	0.56	8	4.7	806.7	70.6
MOF + 8HQ	1	745.6	595.8	0.6	–	–	–	–	–	745.6	59.6
	24	642.8	187.8	0.72	–	–	–	–	–	642.8	43.3
	48	1993	129.8	0.58	93.4	38.2	0.57	5.6	6.5	2086.4	88.7

[a] The standard deviation varied between 5 % and 9 %.

[b] The standard deviation varied between 6 % and 10 %.

[c] The standard deviation varied between 2 % and 6 %.

[d] The standard deviation varied between 5 % and 10 %.

[e] The standard deviation varied between 5 % and 11 %.

[f] The standard deviation varied between 3 % and 6 %.

[g] The standard deviation varied between 4 % and 12 %.

[h] The standard deviation varied between 6 % and 15 %.

[i] The standard deviation varied between 5 % and 10 %.

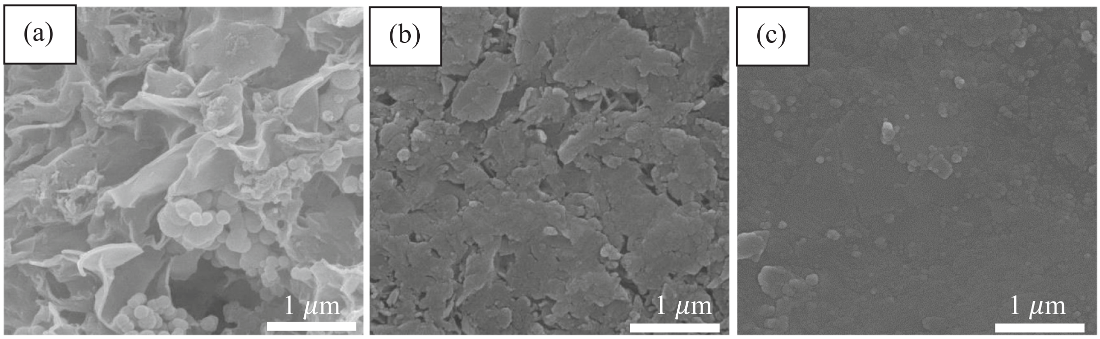

Fig. 10. FESEM micrographs of samples surface immersed in 3.5 % NaCl (a), 3.5 % NaCl containing MOF (b) and MOF + 8HQ extract (c) after 48 h.

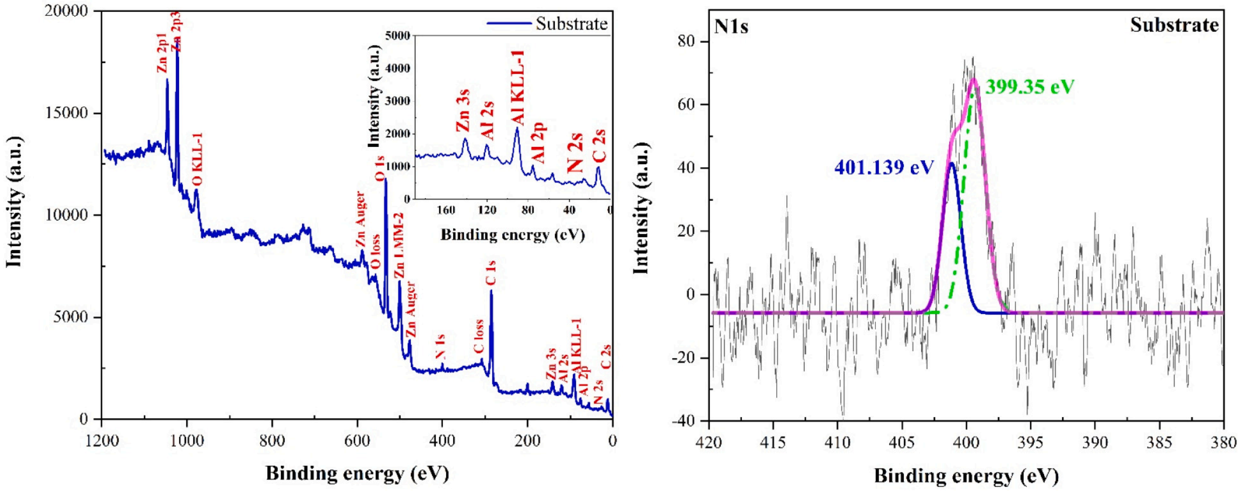

Fig. 11. XPS survey of the sample immersed in MOF + 8HQ extract after immersion for 48 h.

Table 5
Element atom percentages of the sample immersed in MOF + 8HQ extract after immersion for 48 h extracted from XPS survey.

Peak ID	Atom (%)
Zn 2p1	0.8
Zn 2p3	0.6
O KLL-1	4.6
O 1s	3.8
Zn LMM-2	25.7
N 1s	0.2
C 1s	9.1
Zn 3s	1.3
Al 2s	0.7
Al KLL-1	14.8
Al 2p	1.0
N 2s	29.4
C 2s	8.1

(Fig. 10a). The development of an oxide/inhibitive layer on the EGS surface of MOF-containing solutions was confirmed by micrographs. This layer was more compact for the MOF + 8HQ solution compared to the MOF-containing solution. As a result, exposure to the MOF + 8HQ solution formed a densely packed structure film protecting the EGS from corrosion. XPS test was performed to determine the nature of this protective layer. Fig. 11 depicts the XPS survey, and high-resolution XPS patterns of N 1 s of mild steel plates dipped in the test solution containing the MOF + 8HQ. The list of peaks obtained from XPS patterns is presented in Table 5.

The presence of Zn, C, O, Al, and N peaks is obvious in the XPS survey of the EGS plate immersed in the MOF + 8HQ extract, which is related to the liberation of active species from MOF and 8HQ as well as the zinc layer of EGS. In confirmation of this statement, the most common compounds on the surface are N, Zn, and O, indicating the formation/deposition of zinc oxides/hydroxides and precipitation of nitrogen-based complexes over the EGS plate. The existence of two peaks in the deconvoluted spectrum of N 1 s, one at 399.3 eV originating from pyridinic nitrogen of 8HQ [51] and the other one at 401.1 eV attributing to the Zn—N bond [58], is another proof for the prominent role of inhibitor (8HQ) molecules in building the inhibitive layer, which is in good agreement with EIS results.

3.4.2. Single-layer silane coated samples

The MOF and MOF + 8HQ were incorporated into the silane coating, and the coatings corrosion resistance in NaCl solution was investigated by EIS, polarization, and surface analysis experiments. Fig. 12 shows the Bode plots of the coated EGS substrates after 1, 3, 24, 48, and 72 h of immersion and polarization resistance of the sample calculated using Eq. (2) based the real component of the impedance at maximum $Z'(\infty)$ and minimum frequencies $Z'(0)$ [59].

$$R_P = Z'(0) - Z'(\infty) \qquad (2)$$

Bode phase and Nyquist diagrams are provided in the **Supplementary Information** (**Figs. S2** and **S3**).

The majority of silane-coated samples were found to contain two or three-time constants. Each of these time constants is associated with a specific layer of silane coating/oxide layer, and an electrical double layer, as mentioned earlier. The lower high-frequency phase angle value

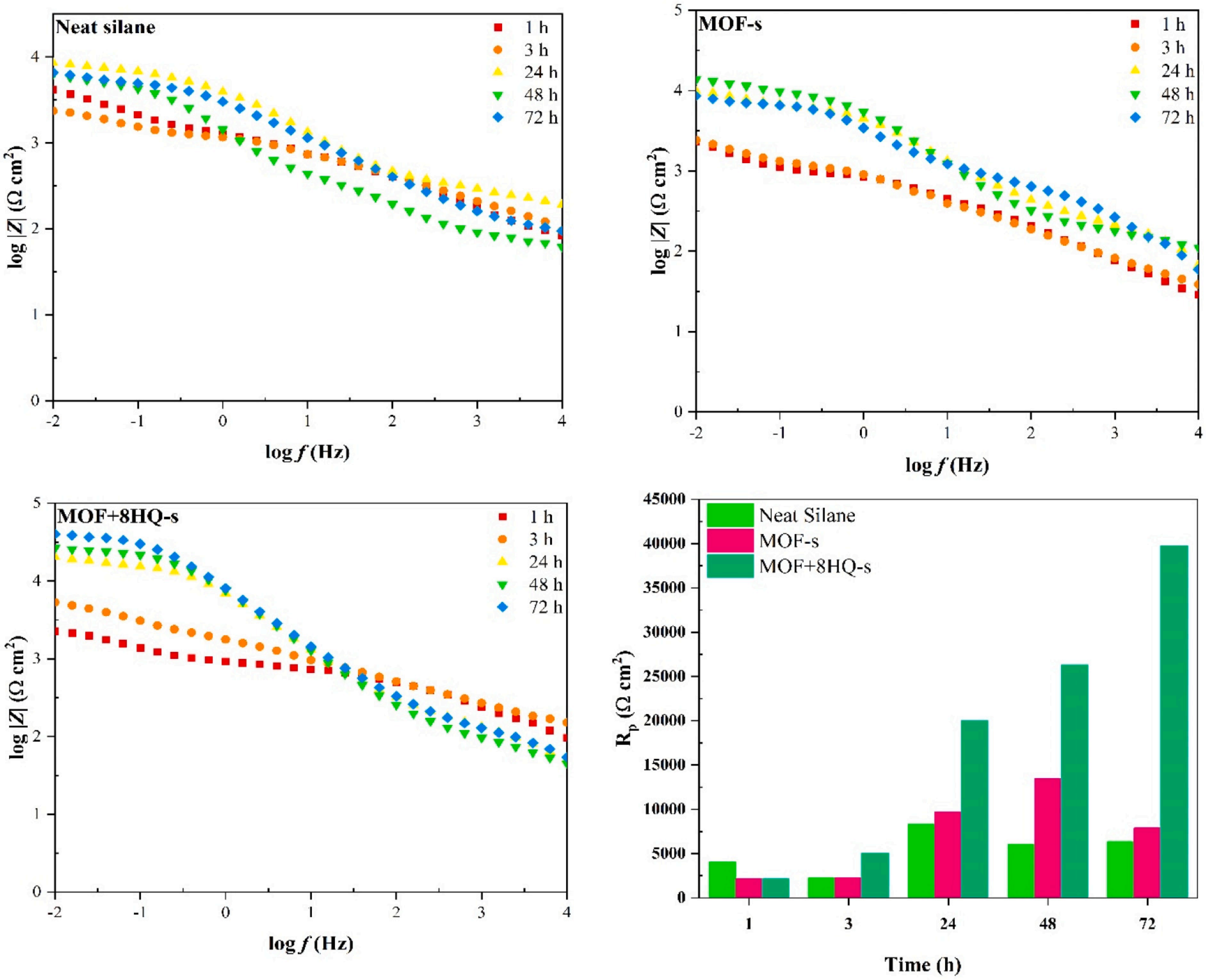

Fig. 12. Bode module and polarization resistance of the silane coated samples for different immersion times.

of the neat silane than MOF-s (silane coating including MOF) and MOF + 8HQ-s (silane coating including MOF + 8HQ) up to 24 h denotes the less barrier action of the neat silane even at early immersion periods. During exposure time (72 h), a significant difference in high-frequency phase angle values occurred for MOF-containing silane samples compared to neat silane, indicating the weak anti-corrosion performance of silane coating in the absence of MOFs. The release of inhibitory species from the MOF + 8HQ structure caused the greatest negative value for MOF + 8HQ-s to be achieved at the end of the exposure period. The BLFI value of the neat silane sample rose up to 24 h, which was primarily assigned to the development of the oxide layer. In the case of MOF-s, the uptrend continued for up to 48 h, and BLFI values were higher than silane, indicating the MOF inhibition power. Due to the presence of 8HQ in the MOF structure and its inhibition role, as well as the ability to form complexes with zinc, the BLFI values for the MOF + 8HQ-s sample have been continuously increased up to 72 h. Consistent with the above findings, the presence of 8HQ also caused a significant change in the Nyquist plots. The MOF + 8HQ-s showed the biggest semicircle diameter at all immersion times, meaning that the corrosion reaction has been significantly reduced.

For the silane without additives, R_P values are appropriate at the beginning of the immersion time and increase to ca. 8.3 kΩ.cm^2 after 24 h. Over time, there was a decline in R_P. It reached ca. 6.4 kΩ.cm^2 at the end of the immersion (72 h). This behavior indicates improper anti-corrosion performance of the neat silane sample during exposure time due to the penetration of electrolytes into the coating. In the case of MOF-s, the highest R_P value was obtained after 48 h (ca. 13.5 kΩ.cm^2), which could be related to the presence of organic ligand in the MOF structure and its interaction with the EGS surface. The highest R_P value was recorded for MOF + 8HQ-s among the samples, which increased over time and eventually reached ca. 39.7 kΩ.cm^2. Such an improvement in protection performance is due to the regular release of the 8HQ into the silane coating (metal/coating interface and/or defect zones).

SEM was employed to assess the surface morphology before exposure to saline solution and the coating thickness (Fig. 13). According to Fig. 13**a1**–**c1**, the inclusion of MOFs in the coatings resulted in a smooth surface, indicating no migration of particles to the coating surface, meaning that the distribution of the particle has occurred through the coating thickness. The thickness of the coatings was about 2.5–3 μm. SEM was also used to examine the state of the silane-coated specimens after 72 h exposure to saline solution, and the outcomes are depicted in Fig. 14. The figures show the occurrence of severe corrosion for neat silane and less corrosion for MOF-s. The least corrosion attacks occurred on the MOF + 8HQ-s sample. All samples showed a tendency to crack after exposure to saline solution. However, the cracks were the least on the MOF + 8HQ-s sample, as per the results of electrochemical tests.

3.4.3. *Duplex (silane + epoxy) coating system*

The Bode impedance module of the scratched duplex coating system on EGS during 72 h immersion in the saline solution is provided in Fig. 15. Bode-phase and Nyquist plots are illustrated in the **Supplementary Information** (**Figs**. **S4** and **S5**). Looking at the figure, the impedance of all coating systems, except the reference sample (blank/epoxy), decreases during exposure to the saline solution, which reflects

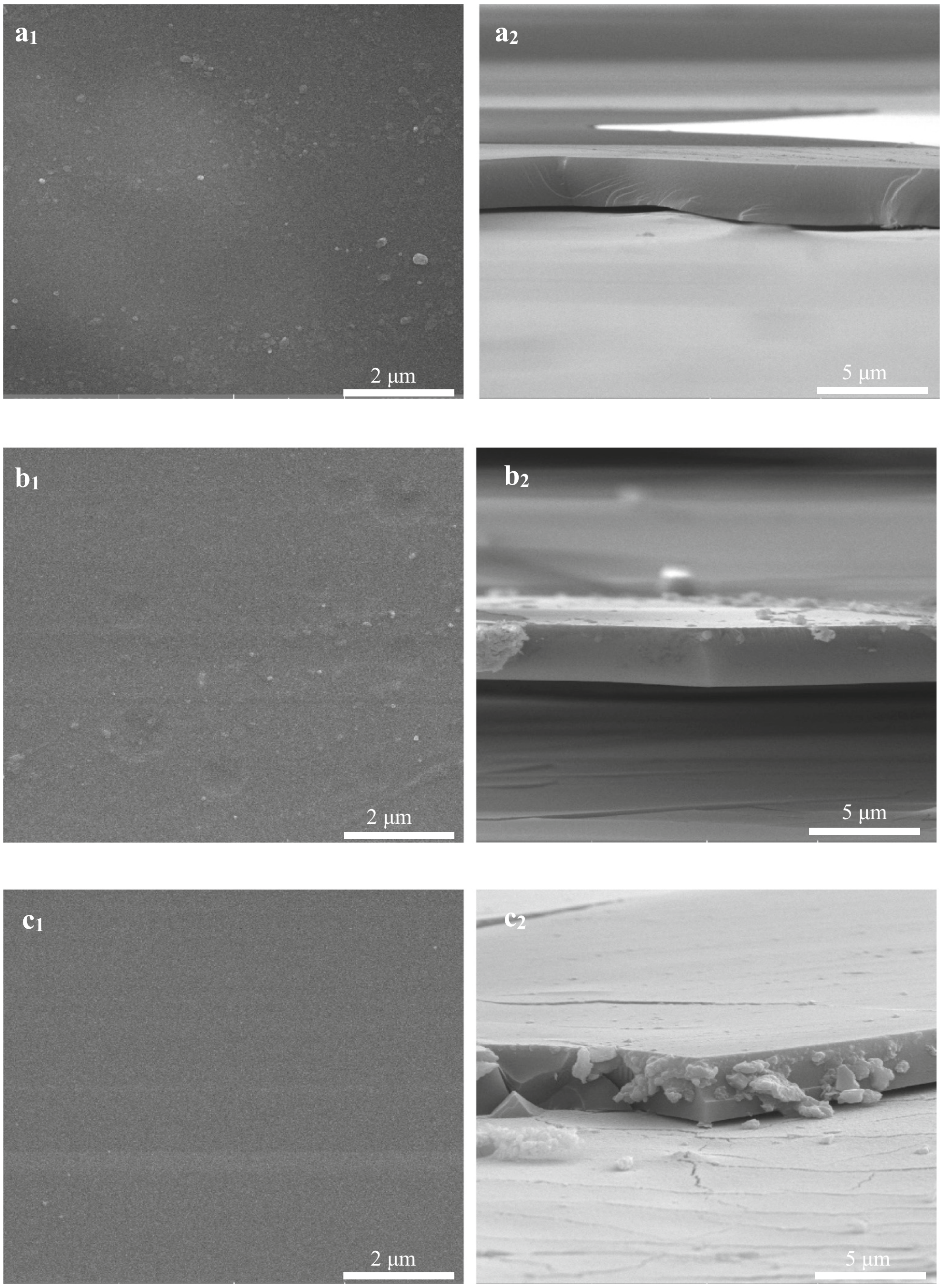

Fig. 13. FESEM micrographs of a: Neat silane, b, MOF-s, c: MOF + 8HQ-s; from the coating surface (a_1, b_1, and c_1) and from the cross-section of the coatings (a_2, b_2, and c_2).

the diffusion of water in the coating-substrate interface and partial detachment of the coating initiating from the scratched area over exposure time. The reference sample shows a partial increment in the corrosion resistance; however, the total resistance is considerably lower compared to the rest of the samples. The low-frequency impedance data are depicted in Fig. 16 to compare different samples better. According to this figure, the application of a silane coating prior to the application of epoxy coating enhanced the corrosion protection properties, which can be originated from the covalent bonding of silane coating to the metal surface. The inclusion of MOF in the silane coating further increased the corrosion protection performance, which can be arisen from the partial dissolution of MOF structure and release of terephthalic acid, leading to the formation of a complex with zinc cations on the EGS surface. The superior protective performance was achieved by the inclusion of 8HQ-doped MOF in the silane coating. Apart from the partial dissolution of MOF, which results in a partial release of 8HQ from 8HQ-doped MOF, 8HQ is mainly released from the MOF due to the concentration gradient as the primary driving force. The released 8HQ from the MOF during the exposure period acts as an effective corrosion inhibitor at the silane-EGS interface.

ECN was also measured from the two nominally identical scratched epoxy-silane duplex coatings. The total energy of the ECN detail crystals for the duplex coating was 70, 44, and 23 nA^2, respectively, for the neat silane, MOF-s, and MOF-8HQ-s. The lowest current noise signal energy associated with epoxy coated MOF-8HQ-s is related to the active corrosion inhibition of released inhibitors in the scratched area. WT was

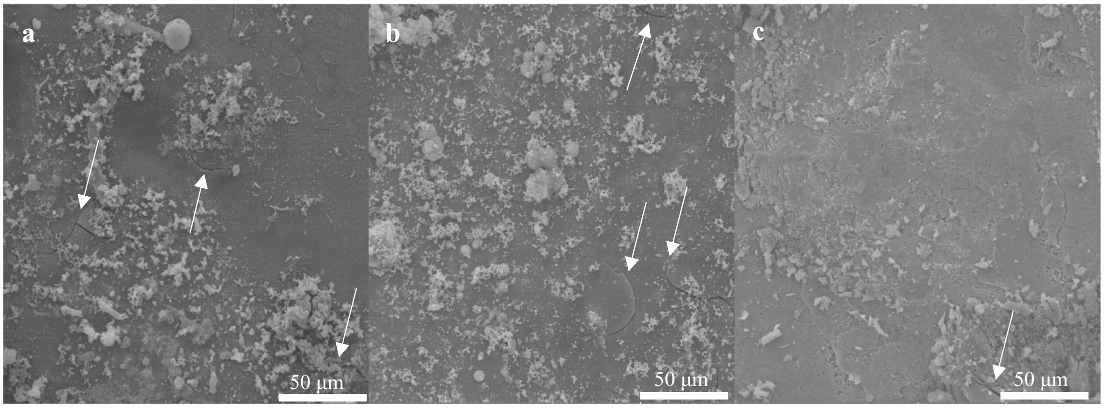

Fig. 14. FESEM micrographs of a: Neat silane, b, MOF-s, c: MOF + 8HQ-s coatings surface after 72 h exposure to 3.5 % NaCl solution. Arrows depict the cracks in the coatings.

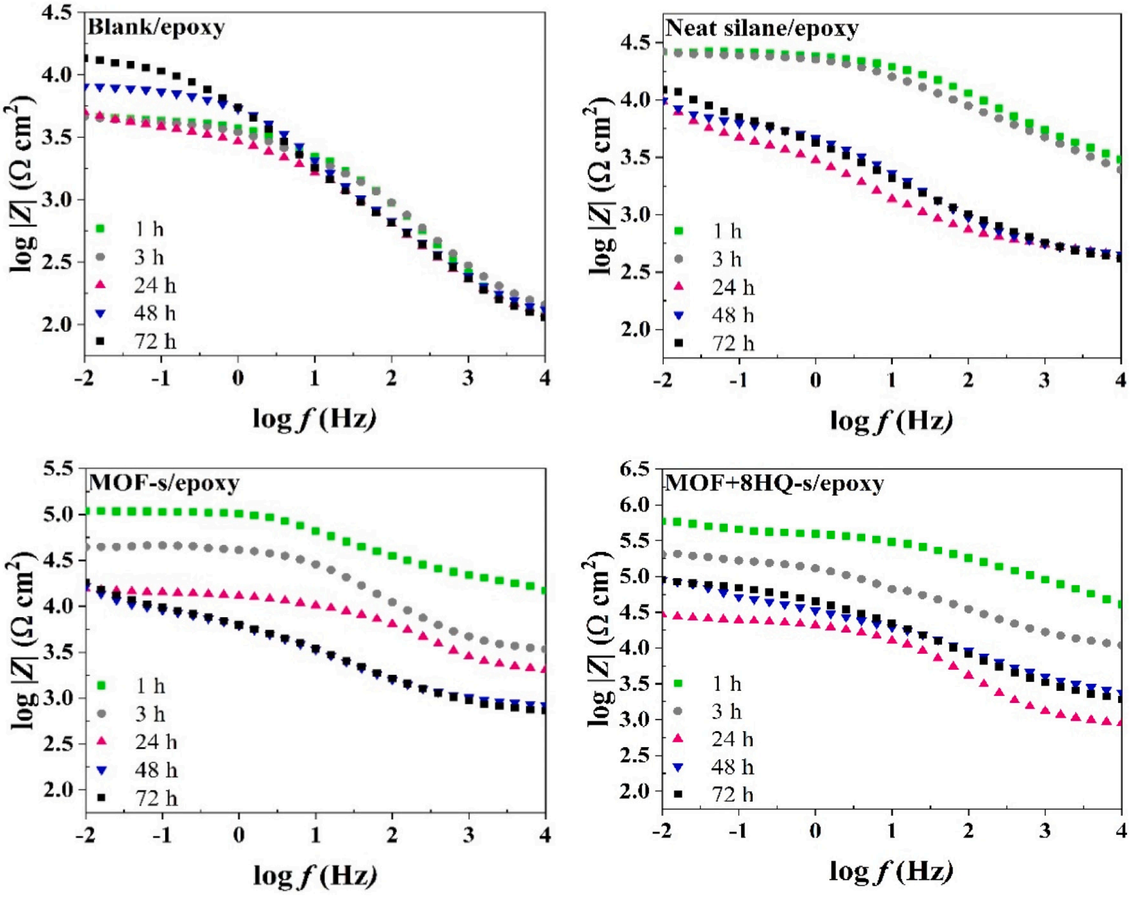

Fig. 15. Bode module diagrams of the scratched dual coating system for different immersion times.

utilized to examine the recorded ECN data. Fig. 17 depicts 3D presentation of WT signals. The original ECN signal with the relative amplitude is provided on the backside of the diagram. Looking at this figure, the epoxy-coated Neat silane and MOF-s samples showed the major parts of transients in the low-frequency region attributed to general corrosion. While epoxy-coated MOF-8HQ-s sample showed a shift of transient to high-frequency regions, indicating changing corrosion mechanism from a general to a localized one. It seems that active inhibitive species have covered the metal surface at the scratched area, and the corrosion occurred at defect areas of the inhibitive film [60].

After removing the coatings, the surface morphology and elemental composition of the surface film were scrutinized by FESEM-EDS. The outcomes are demonstrated in Fig. 18. Looking at the FESEM micrographs, a considerable amount of corrosion products accumulated in the scratched area on the reference (blank/epoxy) sample. The intensity of the corrosion on the neat silane/epoxy and MOF-s/epoxy samples has been decreased compared to the reference sample; however, corrosion attacks around the scratched area are visible. In the case of the MOF + 8HQ-s/epoxy sample, the corrosion attacks are minimal around the scratched region, reflecting its superior protective action compared to the rest of the samples, which is consistent with the EIS results. Looking at the SEM-EDS results from the scratched coating, there is a Fe content

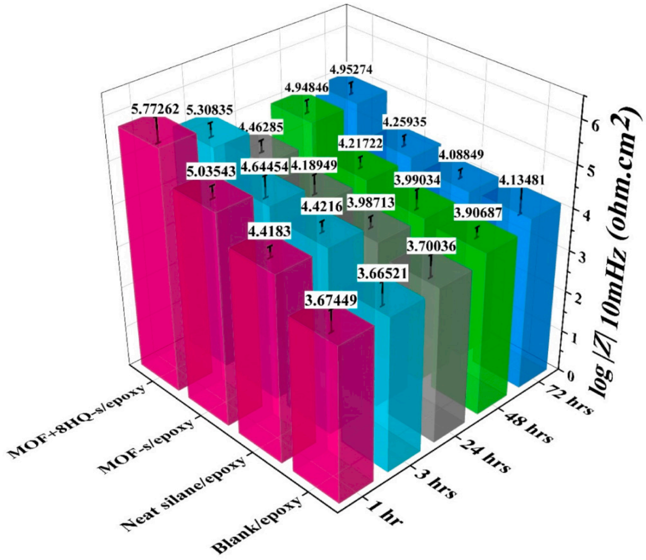

Fig. 16. Low-frequency impedance data of the scratched dual coating systems.

detected on these samples, which means that the zinc layer was also scratched off. This implies the high efficiency of the suggested coating system even when a through defect is formed in the zinc layer, and there is a galvanic coupling between the zinc layer and steel substrate.

4. Conclusion

A MOF based on MIL-53$_{as}$(Al) was synthesized and loaded with 8HQ. The successful loading of 8HQ in MOF was confirmed with FTIR, Raman, XRD, and XPS. The active inhibitive properties of the MOF + 8HQ were revealed in the solution phase on the bare EGS sample. Incorporation of the MOF + 8HQ in the silane coating revealed a significant improvement in the protective functioning of the single-layer silane coating, boosting the total resistance to over 42 k Ω.cm^2 after 72 h immersion in the saline solution. While, after the same period, the as-synthesized MOF-containing silane coating and neat silane coating revealed a total resistance below 10 k Ω.cm^2. In addition, MOF + 8HQ inclusion in the silane coating top-coated with the epoxy coating also revealed an increase in corrosion resistance. The low-frequency impedance of the scratched duplex coating system reached about 100 k Ω.cm^2 in the presence of MOF + 8HQ, while in the presence of as-synthesized MOF and absence of MOF, it was about 15 k Ω.cm^2 and 13 k Ω.cm^2, respectively. The lowest current noise signal energy was obtained in the presence of MOF + 8HQ, further confirming the active corrosion inhibition of released

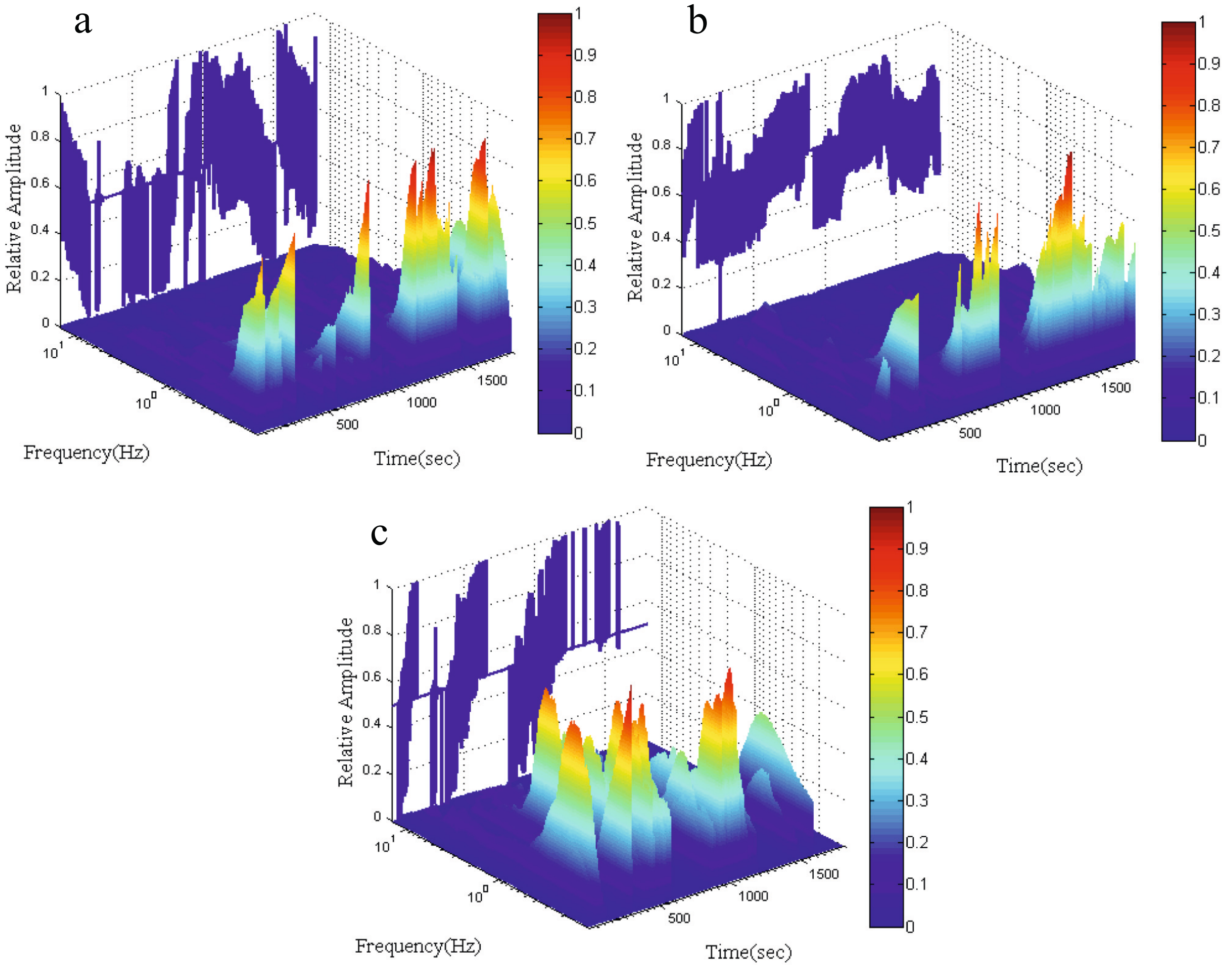

Fig. 17. WT of the ECN data obtained from scratched dual coating systems (a: epoxy coated neat silane, b, epoxy coated MOF-s, c: epoxy coated MOF + 8HQ-s samples) after 72 h exposure to saline solution.

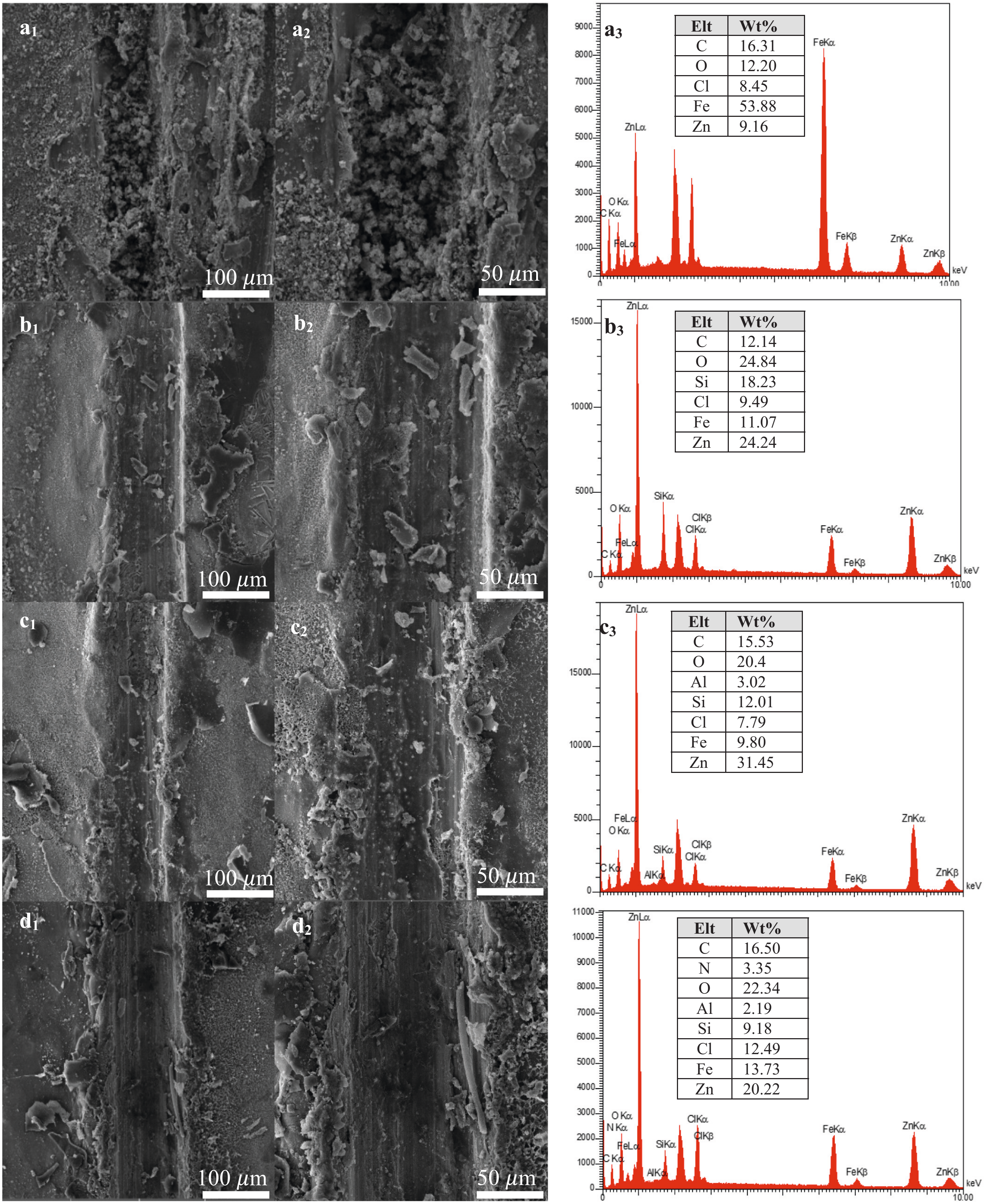

a3

Elt	Wt%
C	16.31
O	12.20
Cl	8.45
Fe	53.88
Zn	9.16

b3

Elt	Wt%
C	12.14
O	24.84
Si	18.23
Cl	9.49
Fe	11.07
Zn	24.24

c3

Elt	Wt%
C	15.53
O	20.4
Al	3.02
Si	12.01
Cl	7.79
Fe	9.80
Zn	31.45

Elt	Wt%
C	16.50
N	3.35
O	22.34
Al	2.19
Si	9.18
Cl	12.49
Fe	13.73
Zn	20.22

Fig. 18. FESEM micrographs and EDX analysis of Blank/epoxy: a_1, a_2 and a_3, Neat silane/epoxy: b_1, b_2 and b_3, MOF-s/epoxy: c_1, c_2 and c_3, MOF + 8HQ-s/epoxy: d_1, d_2 and d_3 after 72 h exposure to the saline solution.

inhibitors in the scratched area. Considering the results obtained in solution and coating phases, the fabricated particles (MOF + 8HQ) can be used to boost the protective functioning of silane coatings.

CRediT authorship contribution statement

M. Mahdavian and M. Olivier supervised the project. S. Akbaripoor Tafreshi Nejad and M. Ramezanzadeh ran the experiments. S. Akbaripoor Tafreshi Nejad, M. Ramezanzadeh, and E. Alibakhshi contributed in preparing the first draft and analysis of the results. M. Mahdavian, M. Olivier, and B. Ramezanzadeh edited the final version of the manuscript.

Declaration of competing interest

The authors declare that they have no known competing financial interests or personal relationships that could have appeared to influence the work reported in this paper.

Data availability

No data was used for the research described in the article.

Appendix A. Supplementary data

Supplementary data to this article can be found online at https://doi.org/10.1016/j.porgcoat.2022.107280.

References

[1] G. Grundmeier, A. Simões, Corrosion protection by organic coatings, in: Encyclopedia of Electrochemistry: Online, 2007, https://doi.org/10.1002/9783527610426.bard040504.

[2] S. Lyon, R. Bingham, D. Mills, Corrosion protection of carbon steel by Pongamia glabra oil-based polyetheramide coatings, Prog. Org. Coat. 102 (2017) 2–7.

[3] O. Boumezgane, R. Suriano, M. Fedel, C. Tonelli, F. Deflorian, S. Turri, Self-healing epoxy coatings with microencapsulated ionic PDMS oligomers for corrosion protection based on supramolecular acid-base interactions, Prog. Org. Coat. (2022) 162 106558, https://doi.org/10.1016/j.porgcoat.2021.106558.

[4] M.L. Zheludkevich, D.G. Shchukin, K.A. Yasakau, H. Möhwald, M.G. Ferreira, Anticorrosion coatings with self-healing effect based on nanocontainers impregnated with corrosion inhibitor, Chem. Mater. 19 (3) (2007) 402–411, https://doi.org/10.1021/cm062066k.

[5] M. Ramezanzadeh, B. Ramezanzadeh, M. Mahdavian, G. Bahlakeh, Development of metal-organic framework (MOF) decorated graphene oxide nanoplatforms for anti-corrosion epoxy coatings, Carbon 161 (2020) 231–251.

[6] Y. Wu, F. Jiang, Y. Qiang, W. Zhao, Synthesizing a novel fluorinated reduced graphene oxide-CeO2 hybrid nanofiller to achieve highly corrosion protection for waterborne epoxy coatings, Carbon 176 (2021) 39–51, https://doi.org/10.1016/j.carbon.2021.01.135.

[7] G. Cai, S. Xiao, C. Deng, D. Jiang, X. Zhang, Z. Dong, CeO2 grafted carbon nanotube via polydopamine wrapping to enhance corrosion barrier of polyurethane coating, Corros. Sci. (2021) 178 109014, https://doi.org/10.1016/j.corsci.2020.109014.

[8] M. Rui, Y. Jiang, A. Zhu, Sub-micron calcium carbonate as a template for the preparation of dendrite-like PANI/CNT nanocomposites and its corrosion protection properties, Chem. Eng. J. (2019), 123396, https://doi.org/10.1016/j.cej.2019.123396.

[9] R.G. Buchheit, H. Guan, S. Mahajanam, F. Wong, Active corrosion protection and corrosion sensing in chromate-free organic coatings, Progress in Organic Coatings 47 (3–4) (2003) 174–182, https://doi.org/10.1016/j.porgcoat.2003.08.003.

[10] E. Alibakhshi, E. Ghasemi, M. Mahdavian, B. Ramezanzadeh, Corrosion inhibitor release from Zn-Al-[PO43-]-[CO32-] layered double hydroxide nanoparticles, Prog. Color Color. Coat. 9 (4) (2016) 233–248. https://dx.doi.org/10.30509/pccc.2016.75889.

[11] S.A. Haddadi, M. Amini, S. Ghaderi, A.R. SA, Synthesis and cation-exchange behavior of expanded MoS2 nanosheets for anticorrosion applications, Materials Today: Proceedings 5 (7) (2018) 15573–15579, https://doi.org/10.1016/j.matpr.2018.04.165.

[12] X. Li, X. Liu, H. Liu, X. Liu, R. He, S. Meng, Structure, morphology and anti-corrosion performance of polyaniline modified molybdenum sulfide/epoxy composite coating, Colloids and Surfaces A: Physicochemical and Engineering Aspects (2022) 128345, https://doi.org/10.1016/j.colsurfa.2022.128345.

[13] M. Zhang, X. Yu, Y. Lin, J. Liu, J. Wang, Anti-corrosion coatings with active and passive protective performances based on v-COF/GO nanocontainers, Prog. Org. Coat. (2021) 159 106415, https://doi.org/10.1016/j.porgcoat.2021.106415.

[14] C. Zhang, W. Li, C. Liu, et al., Effect of covalent organic framework modified graphene oxide on anticorrosion and self-healing properties of epoxy resin coatings, J. Colloid Interface Sci. (2021), https://doi.org/10.1016/j.jcis.2021.10.024.

[15] H. Yan, L. Zhang, H. Li, X. Fan, M. Zhu, Towards high-performance additive of Ti3C2/graphene hybrid with a novel wrapping structure in epoxy coating, Carbon 157 (2020) 217–233, https://doi.org/10.1016/j.carbon.2019.10.034.

[16] S.A. Haddadi, S. Hu, S. Ghaderi, et al., Amino-functionalized MXene nanosheets doped with ce (III) as potent nanocontainers toward self-healing epoxy nanocomposite coating for corrosion protection of mild steel, ACS Appl. Mater. Interfaces (2021), https://doi.org/10.1021/acsami.1c13055.

[17] N.A. Ismail, A.M. Moussa, R. Kahraman, R. Shakoor, Study on the corrosion behavior of polymeric nanocomposite coatings containing halloysite nanotubes loaded with multicomponent inhibitor, Arab. J. Chem. 15 (9) (2022), 104107, https://doi.org/10.1016/j.arabjc.2022.104107.

[18] M. Ramezanzadeh, B. Ramezanzadeh, Thermomechanical and Anticorrosion Characteristics of Metal-organic Frameworks, Elsevier, 2021.

[19] A.U. Czaja, N. Trukhan, U. Müller, Industrial applications of metal–organic frameworks, Chem. Soc. Rev. 38 (5) (2009) 1284–1293, https://doi.org/10.1039/B804680H.

[20] E. Tomic, Thermal stability of coordination polymers, J. Appl. Polym. Sci. 9 (11) (1965) 3745–3752, https://doi.org/10.1002/app.1965.070091121.

[21] O.M. Yaghi, M. O'Keeffe, N.W. Ockwig, H.K. Chae, M. Eddaoudi, J. Kim, Reticular synthesis and the design of new materials, Nature 423 (6941) (2003) 705–714, https://doi.org/10.1038/nature01650.

[22] U. Mueller, M. Schubert, F. Teich, H. Puetter, K. Schierle-Arndt, J. Pastre, Metal–organic frameworks—prospective industrial applications, J. Mater. Chem. 16 (7) (2006) 626–636, https://doi.org/10.1039/B511962F.

[23] M.H. Nazari, Y. Zhang, A. Mahmoodi, et al., Nanocomposite organic coatings for corrosion protection of metals: a review of recent advances, Prog. Org. Coat. (2022) 162 106573, https://doi.org/10.1016/j.porgcoat.2021.106573.

[24] C. Liu, B. Qian, P. Hou, Z. Song, Stimulus responsive zeolitic imidazolate framework to achieve corrosion sensing and active protecting in polymeric coatings, ACS Appl. Mater. Interfaces 13 (3) (2021) 4429–4441, https://doi.org/10.1021/acsami.0c22642.

[25] Y. Zhao, T. Xu, J.-H. Zhou, J.-M. Hu, Superhydrophobic nanocontainers for passive and active corrosion protection, Chem. Eng. J. (2021), 134039, https://doi.org/10.1016/j.cej.2021.134039.

[26] Y. Wang, J. Hu, Y. Ma, et al., A novel high-efficient MOFs-based corrosion inhibitor for the reinforcing steel in cement extract, Constr. Build. Mater. (2022) 317 125946, https://doi.org/10.1016/j.conbuildmat.2021.125946.

[27] A.E.-A.S. Fouda, S.E.H. Etaiw, G.S. Hassan, Chemical, electrochemical and surface studies of new metal–organic frameworks (MOF) as corrosion inhibitors for carbon steel in sulfuric acid environment, Sci. Rep. 11 (1) (2021) 1–16, https://doi.org/10.1038/s41598-021-99700-3.

[28] J. Zhao, W.T. Nunn, P.C. Lemaire, et al., Facile conversion of hydroxy double salts to metal–organic frameworks using metal oxide particles and atomic layer deposition thin-film templates, J. Am. Chem. Soc. 137 (43) (2015) 13756–13759, https://doi.org/10.1021/jacs.5b08752.

[29] A.J. Cruz, I. Stassen, M. Krishtab, et al., Integrated cleanroom process for the vapor-phase deposition of large-area zeolitic imidazolate framework thin films, Chem. Mater. 31 (22) (2019) 9462–9471, https://doi.org/10.1021/acs.chemmater.9b03435.

[30] S. Duan, B. Dou, X. Lin, et al., Influence of active nanofiller ZIF-8 metal-organic framework (MOF) by microemulsion method on anticorrosion of epoxy coatings, Colloids Surf. A Physicochem. Eng. Asp. (2021) 624 126836, https://doi.org/10.1016/j.colsurfa.2021.126836.

[31] M. Ramezanzadeh, B. Ramezanzadeh, G. Bahlakeh, A. Tati, M. Mahdavian, Development of an active/barrier bi-functional anti-corrosion system based on the epoxy nanocomposite loaded with highly-coordinated functionalized zirconium-based nanoporous metal-organic framework (Zr-MOF), Chem. Eng. J. (2021) 408 127361, https://doi.org/10.1016/j.cej.2020.127361.

[32] Y. Zhao, F. Jiang, Y.-Q. Chen, J.-M. Hu, Coatings embedded with GO/MOFs nanocontainers having both active and passive protecting properties, Corros. Sci. (2020) 108563, https://doi.org/10.1016/j.corsci.2020.108563.

[33] H. Chen, Z. Yu, K. Cao, et al., Preparation of a BTA–UIO–GO nanocomposite to endow coating systems with active inhibition and passive anticorrosion performances, New J. Chem. (2021), https://doi.org/10.1039/D1NJ03104J.

[34] I.A. Kartsonakis, S.G. Stanciu, A.A. Matei, R. Hristu, A. Karantonis, C.A. Charitidis, A comparative study of corrosion inhibitors on hot-dip galvanized steel, Corros. Sci. 112 (2016) 289–307, https://doi.org/10.1016/j.corsci.2016.07.030.

[35] M. Taryba, S. Lamaka, D. Snihirova, et al., The combined use of scanning vibrating electrode technique and micro-potentiometry to assess the self-repair processes in defects on "smart" coatings applied to galvanized steel, Electrochim. Acta 56 (12) (2011) 4475–4488, https://doi.org/10.1016/j.electacta.2011.02.048.

[36] M. Wang, J. Wang, W. Hu, Preparation and corrosion behavior of cu-8-HQ@HNTs/epoxy coating, Prog. Org. Coat. (2020) 139 105434.

[37] Y. An, H. Li, Y. Liu, et al., Photoelectrical, photophysical and photocatalytic properties of Al based MOFs: MIL-53 (Al) and MIL-53-NH2 (Al), J. Solid State Chem. 233 (2016) 194–198, https://doi.org/10.1016/j.jssc.2015.10.037.

[38] S.Akbaripoor Tafreshi Nejad, E. Alibakhshi, B. Ramezanzadeh, F. Marhamati, M.-G. Olivier, M. Mahdavian, The role of acetylacetone in alkaline surface modification bath of electro-galvanized steel to enhance protective functioning of a hybrid silane coating, Progress in Organic Coatings 171 (2022) 107048, https://doi.org/10.1016/j.porgcoat.2022.107048.

[39] T. Loiseau, C. Volkringer, M. Haouas, F. Taulelle, G. Férey, Crystal chemistry of aluminium carboxylates: from molecular species towards porous infinite three-

dimensional networks, C. R. Chim. 18 (12) (2015) 1350–1369, https://doi.org/10.1016/j.crci.2015.08.006.
[40] E. M. Ales, Characterization of metal-biomass interactions in the lanthanum (III) biosorption on Sargassum sp using SEM/EDX, FTIR, and XPS: Preliminary studies.
[41] R.C. Tacker, Hydroxyl ordering in igneous apatite, Am. Mineral. 89 (10) (2004) 1411–1421, https://doi.org/10.2138/am-2004-1008.
[42] H. Xiao, W. Zhang, Q. Yao, et al., Zn-free MOFs like MIL-53 (Al) and MIL-125 (Ti) for the preparation of defect-rich, ultrafine ZnO nanosheets with high photocatalytic performance, Appl. Catal. B Environ. 244 (2019) 719–731, https://doi.org/10.1016/j.apcatb.2018.11.026.
[43] K. Shetty, K. Raj, N. Mohan, Synthesis, characterization and corrosion studies of polyanailine (PANI)/ceriem dioxide (CeO2) nano composite, Mater. Today: Proc. 27 (2020) 2158–2163, https://doi.org/10.1016/j.matpr.2019.09.087.
[44] F. Doğan, İ. Kaya, K. Temizkan, Chemical oxidative synthesis and characterization of poly (8-hydroxyquinoline) particles, J. Macromol. Sci. A 51 (12) (2014) 948–961, https://doi.org/10.1080/10601325.2014.967081.
[45] Y. Chen, B. Ren, S. Gao, R. Cao, The sandwich-like structures of polydopamine and 8-hydroxyquinoline coated graphene oxide for excellent corrosion resistance of epoxy coatings, J. Colloid Interface Sci. 565 (2020) 436–448, https://doi.org/10.1016/j.jcis.2020.01.051.
[46] M.K. Fung, A.M.C. Ng, A.B. Djurišić, W.K. Chan, H. Wang, Preparation of 8-hydroxyquinoline wires by decomposition of tris (8-hydroxyquinoline) aluminium, J. Exp. Nanosci. 7 (5) (2012) 578–585, https://doi.org/10.1080/17458080.2010.543992.
[47] L. Bistričić, V. Borjanović, M. Leskovac, et al., Raman spectra, thermal and mechanical properties of poly (ethylene terephthalate) carbon-based nanocomposite films, J. Polym. Res. 22 (3) (2015) 1–12, https://doi.org/10.1007/s10965-015-0680-z.
[48] M. Sowa, M. Wala, A. Blacha-Grzechnik, et al., Corrosion inhibitor-modified plasma electrolytic oxidation coatings on 6061 aluminum alloy, Materials 14 (3) (2021) 619, https://doi.org/10.3390/ma14030619.
[49] X.Y. Chen, V.-T. Hoang, D. Rodrigue, S. Kaliaguine, Optimization of continuous phase in amino-functionalized metal–organic framework (MIL-53) based co-polyimide mixed matrix membranes for CO 2/CH 4 separation, RSC Adv. 3 (46) (2013) 24266–24279, https://doi.org/10.1039/C3RA43486A.
[50] I. Kartsonakis, I. Daniilidis, G. Kordas, Encapsulation of the corrosion inhibitor 8-hydroxyquinoline into ceria nanocontainers, J. Sol-Gel Sci. Technol. 48 (1) (2008) 24–31, https://doi.org/10.1007/s10971-008-1810-4.
[51] M. Jing, T. Wu, Y. Zhou, X. Li, Y. Liu, Nitrogen-doped graphene via in-situ alternating voltage electrochemical exfoliation for supercapacitor application, Front. Chem. (2020) 8 428, https://doi.org/10.3389/fchem.2020.00428.
[52] J.A.P. Taborda, H.R. Landázuri, L.P.V. Londoño, Correlation between optical, morphological, and compositional properties of aluminum nitride thin films by pulsed laser deposition, IEEE Sensors J. 16 (2) (2015) 359–364, https://doi.org/10.1109/JSEN.2015.2466467.
[53] M. Razizadeh, M. Mahdavian, B. Ramezanzadeh, E. Alibakhshi, S. Jamali, Synthesis of hybrid organic–inorganic inhibitive pigment based on basil extract and zinc cation for application in protective construction coatings, Constr. Build. Mater. (2021) 287 123034, https://doi.org/10.1016/j.conbuildmat.2021.123034.
[54] A. Salmasifar, M. Edraki, E. Alibakhshi, B. Ramezanzadeh, G. Bahlakeh, Combined electrochemical/surface investigations and computer modeling of the aquatic artichoke extract molecules corrosion inhibition properties on the mild steel surface immersed in the acidic medium, J. Mol. Liq. (2021) 327 114856, https://doi.org/10.1016/j.molliq.2020.114856.
[55] M.E.H.N. Tehrani, M. Ramezanzadeh, B. Ramezanzadeh, A highly-effective/durable metal-organic anti-corrosion film deposition on mild steel utilizing Malva sylvestris (MS) phytoextract-divalent zinc cations, J. Ind. Eng. Chem. 95 (2021) 292–304, https://doi.org/10.1016/j.jiec.2021.01.002.
[56] X. Yao, Y. Lai, F. Huang, Y. Qiang, Y. Jin, 5, 5′-dithiobis-(2-nitrobenzoic acid) self-assembled monolayer for corrosion inhibition of copper in sodium chloride solution, J. Mol. Liq. (2021) 343 117535, https://doi.org/10.1016/j.molliq.2021.117535.
[57] M. Talebian, K. Raeissi, M. Atapour, et al., Inhibitive effect of sodium (E)-4-(4-nitrobenzylideneamino) benzoate on the corrosion of some metals in sodium chloride solution, Appl. Surf. Sci. 447 (2018) 852–865.
[58] S. Yang, Y. Wang, H. Li, et al., Synthesis of nano-ZIF-8@ chitosan microspheres and its rapid removal of p-hydroxybenzoic acid from the agro-industry and preservatives, J. Porous. Mater. 28 (1) (2021) 29–38, https://doi.org/10.1007/s10934-020-00966-1.
[59] M. Meeusen, L. Zardet, A. Homborg, et al., The effect of time evolution and timing of the electrochemical data recording of corrosion inhibitor protection of hot-dip galvanized steel, Corros. Sci. (2020) 173 108780, https://doi.org/10.1016/j.corsci.2020.108780.
[60] E. Alibakhshi, E. Ghasemi, M. Mahdavian, B. Ramezanzadeh, S. Farashi, Active corrosion protection of mg-Al-PO43− LDH nanoparticle in silane primer coated with epoxy on mild steel, J. Taiwan Inst. Chem. Eng. 75 (2017) 248–262, https://doi.org/10.1016/j.jtice.2017.03.010.